Title	RF front-end architecture for a triple-band CMOS GPS receiver
Author(s)	Jo, Ikkyun; Bae, Jungnam; Matsuoka, Toshimasa et al.
Citation	Microelectronics Journal. 2015, 46(1), p. 27-35
Version Type	VoR
URL	https://hdl.handle.net/11094/51675
rights	© 2014 The Authors. Published by Elsevier Ltd. This article is licensed under a Creative Commons Attribution-NonCommercial-NoDerivs 3.0 Unported License.
Note	

RF front-end architecture for a triple-band CMOS GPS receiver

Ikkyun Jo [a,*], Jungnam Bae [a], Toshimasa Matsuoka [a], Takuji Ebinuma [b]

[a] Department of Electrical, Electronic and Information Engineering, Graduate School of Engineering, Osaka University, 2-1 Yamada-oka, Suita, Osaka 565-0871, Japan
[b] Department of Aeronautics and Astronautics, Graduate School of Engineering, University of Tokyo, 7-3-1 Hongo, Bunkyo-ku, Tokyo 113-8656, Japan

A B S T R A C T

This paper describes a triple-band global positioning system (GPS) receiver that simultaneously covers the L1, L2, and L5 frequency bands. The proposed receiver uses an image-rejection technique that can separate signals from the three frequency bands to three corresponding ports. It uses a single RF path containing a low-noise amplifier (LNA), and active and passive mixers with a pair of local oscillator signals. A triple-band GPS RF front-end chip was fabricated using 130 nm CMOS technology. The noise figure of this chip is less than 7 dB and its S_{11} coefficient is less than -10 dB in the 1.15-1.6 GHz frequency range. The power consumption of the LNA and mixers is 7.2 mW when using a 1.2 V supply voltage. The image-rejection ratio (IMRR) between L1 and the other (L2 and L5) band signals is 40 dB, while that between the L2 and L5 signals is 37–38 dB. To improve the IMRR between the L2 and L5 signals, we investigated the utilization of a digital compensation technique. This technique was confirmed to have improved the IMRR by about 12 dB.

1. Introduction

Recently, the global positioning system (GPS), which was originally developed for military purposes, is widely used to obtain location information for applications such as car navigation systems. The widespread use of civilian GPS signals in consumer applications has been promoted by the development of a single GPS receiver chip fabricated in a CMOS process, since its size, cost, and power consumption have been significantly reduced [1]. Conversely, the use of civilian GPS signals is also becoming attractive for scientific applications, such as ocean remote sensing [2], in which higher positioning accuracy is required. One way of achieving this accuracy is to use multiple civilian GPS signals at different frequencies, and such an approach can also offer advantages for robust GPS services such as those used in aviation. Multi-band GPS has come closer to reality with the launch of a satellite that transmits in the L5 band, which compliments the L1 and L2 civilian bands that are currently in use [3]. Thus, GPS receivers that can detect all three bands simultaneously are now in high demand.

One of the key issues in designing a triple-band GPS receiver is how to implement a highly integrated RF front-end that can operate at low power consumption. To date, very few multi-band GPS receivers have been developed [4–10]. Although dual-band receivers that have good signal isolation and use a band-selection architecture [6] or a simple parallel arrangement of several receivers [8,9] have

been developed, these approaches cannot lead to the development of compact low-power low-cost devices. Simultaneous reception with the same RF signal delay, which is important for some scientific applications [2], is possible only in dual-band receivers [4,5,7,10], not in triple-band receivers. To achieve a compact low-power triple-band GPS receiver with such reception, the signal separation for the three band signals on the single RF signal is a key technique.

In this study, we propose architecture for a triple-band GPS receiver that can simultaneously receive the L1, L2, and L5 frequency bands. The RF front-end designed and fabricated for the proposed receiver by using 130 nm CMOS technology was evaluated only on the chip-level in the previous work [11]. This paper focuses more on the evaluation of system levels by using a module with an RF front-end chip as well as the external matching circuit and commercial A/D converters. The RF front-end chip has a wide-band low-noise amplifier (LNA) with a low noise figure (NF) and input matching (S_{11}) in the 1.15–1.6 GHz frequency range, and uses active and passive mixers for modified Weaver image-rejection [12,13]. In the proposed architecture, the L1 band signal is received though a single poly phase filter (PPF), while the other signals (L2 and L5) are received from two PPFs. Therefore, the image-rejection ratio (IMRR) between the L2 and L5 band signals becomes worse than that between the L2 or L5 and L1 band signals. To improve this issue with the IMRR, a digital compensation technique was also investigated.

The remainder of this paper is organized as follows. The proposed architecture of the RF front-end separating each of the received signals simultaneously is described in Section 2. The

* Corresponding author.
  E-mail address: jo@si.eei.eng.osaka-u.ac.jp (I. Jo).

blocks of the proposed RF front-end chip are shown in Section 3. The measurement results of the designed chip are presented in Section 4. In Section 5, the compensation technique to improve the IMRR between the L2 and L5 band signals is discussed. A conclusion is given in the final section.

2. Principle of the proposed receiver architecture

The proposed triple-band receiver architecture is shown in Fig. 1. It can receive each band signal through a single RF front-end by using the Weaver image-rejection method. The architecture is basically modified from that of a dual-band GPS receiver developed in a previous study [12,13]. In the current structure, triple-band signals can be received at each port through a proper phase conversion of each band signal. Furthermore, by adequately setting the LO1 and LO2 frequencies, it can receive each of the band signals without changing the LO signals. The PPFs between the main blocks in Fig. 1 convert the phases of each signal. By applying the above process, the undesired signals can be removed with Weaver image-rejection. Undesired signals are image signals with respect to the desired signal.

The Weaver image-rejection method separates the L1 band signal from the L2 and L5 band signals, which are image signals with respect to the L1 band signal. Then, the PPFs convert the phase of the L2 and L5 band signals and create one signal as an image signal with respect to the other signal. Thus, each band signal can be received independently at each port.

For a more detailed explanation, the flow of the signal processing of the receiver is shown in Fig. 2. For the image-rejection method, the concept of complex signal processing and the Hilbert transform (denoted as "H" in the figure) were used to give concise expressions [14,15].

The RF input signal can be expressed as

$$s_{RF}(t) = \Re[a(t) \exp(j\omega t)], \tag{1}$$

where $a(t)$ is a complex base-band signal and ω is the angular frequency of the RF signal. The frequency and phase of this RF signal are converted along with the quadrature LO signals in the first-stage mixer as follows:

$$s_{RF}(t)\, e^{-j\omega_{LO1}t} = \tfrac{1}{2}[a(t)e^{j(\omega - \omega_{LO1})t} + a^*(t)e^{-j(\omega + \omega_{LO1})t}]. \tag{2}$$

The first term in the brackets on the right-hand side is the desired down-converted component. The first PPFs generate the Hilbert transforms of the real and imaginary components of their input signals to change their phases [15]. The resulting outputs consisting of four differential pairs are intertwined to cancel the undesired band signals, which is implemented by using proper resistive adders. As the transfer function of the Hilbert transform is $-j\,\mathrm{sgn}(\omega)$, where $\mathrm{sgn}(\omega)$ is the sign function, these intertwined signals can be expressed as [11]

$$
\begin{aligned}
s_{IF1,I}(t) = &\ \Re[a(t)e^{j(\omega - \omega_{LO1})t}]u(\omega_{LO1} - \omega) \\
&+ \Im[a(t)e^{j(\omega - \omega_{LO1})t}]u(\omega - \omega_{LO1}) \\
&+ \Re[a(t)e^{j(\omega + \omega_{LO1})t}]
\end{aligned} \tag{3}
$$

$$
\begin{aligned}
s_{IF1,Q}(t) = &\ -\Im[a(t)e^{j(\omega - \omega_{LO1})t}]u(\omega_{LO1} - \omega) \\
&+ \Re[a(t)e^{j(\omega - \omega_{LO1})t}]u(\omega - \omega_{LO1}) \\
&+ \Im[a(t)e^{j(\omega + \omega_{LO1})t}].
\end{aligned} \tag{4}
$$

where $u(\omega)(= (1 + \mathrm{sgn}(\omega))/2)$ is the step function. Note that the frequency components of $\omega - \omega_{LO1}$ in $s_{IF1,I}(t)$ and $s_{IF1,Q}(t)$ have opposite polarity and both have opposite polarity for $\omega > \omega_{LO1}$ and $\omega < \omega_{LO1}$. These features are useful for the signal separation between L1 and the other (L2 and L5) band signals.

The obtained signals that had their frequency and phase translated via the above process are converted again in the second-stage mixer. Here the quadrature LO signals of the LO frequency $f_{LO2}(= \omega_{LO2}/2\pi)$ are used to convert the phase and frequency. To separate L1 and the other signals, the outputs of the second mixers are properly added and subtracted to extract the L1 band signal and to generate the combinations of the L2 and L5 band signals with different polarity, such as follows:

$$
\begin{aligned}
s_{IF2,L1}(t) = &\ -\Im[s_{IF1,I}(t)e^{-j\omega_{LO2}t}] + \Re[s_{IF1,Q}(t)e^{-j\omega_{LO2}t}] \\
= &\ \Re[a(t)e^{j(\omega - \omega_{LO1} - \omega_{LO2})t}]u(\omega - \omega_{LO1}) \\
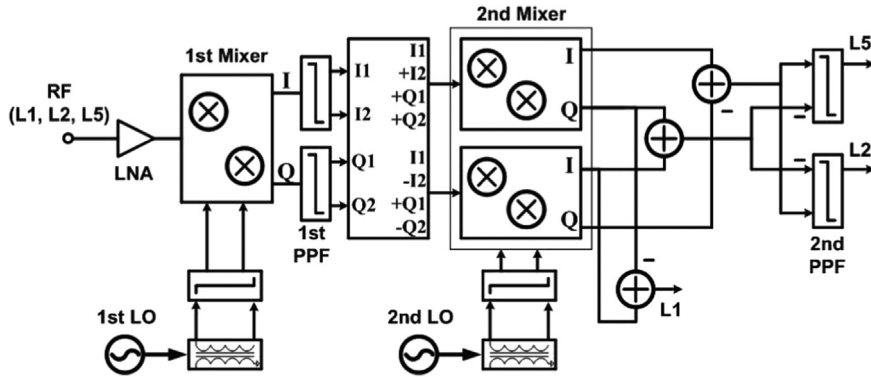&- \Im[a(t)e^{j(\omega - \omega_{LO1} - \omega_{LO2})t}]u(\omega_{LO1} - \omega)
\end{aligned} \tag{5}
$$

Fig. 1. Proposed triple-band receiver.

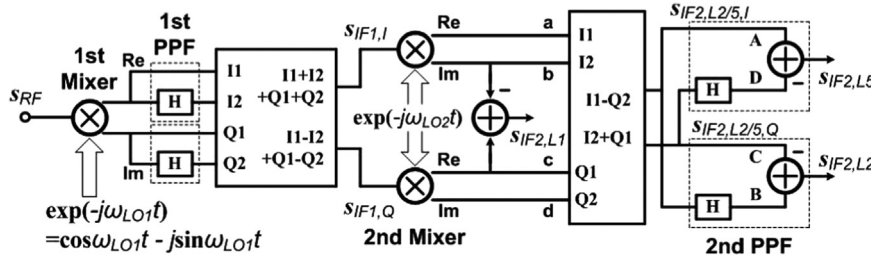**Fig. 2.** Signal processing of the proposed triple-band receiver shown in Fig. 1.

$$s_{IF2,L2/5,I}(t) = \Re[s_{IF1,I}(t)e^{-j\omega_{LO2}t}] - \Im[s_{IF1,Q}(t)e^{-j\omega_{LO2}t}]$$
$$= \Im[a(t)e^{j(\omega-\omega_{LO1}+\omega_{LO2})t}]u(\omega-\omega_{LO1})$$
$$+ \Re[a(t)e^{j(\omega-\omega_{LO1}+\omega_{LO2})t}]u(\omega_{LO1}-\omega)$$
$$+ \Re[a(t)e^{j(\omega+\omega_{LO1}-\omega_{LO2})t}] \quad (6)$$

$$s_{IF2,L2/5,Q}(t) = \Im[s_{IF1,I}(t)e^{-j\omega_{LO2}t}] + \Re[s_{IF1,Q}(t)e^{-j\omega_{LO2}t}]$$
$$= \Re[a(t)e^{j(\omega-\omega_{LO1}+\omega_{LO2})t}]u(\omega-\omega_{LO1})$$
$$- \Im[a(t)e^{j(\omega-\omega_{LO1}+\omega_{LO2})t}]u(\omega_{LO1}-\omega)$$
$$+ \Im[a(t)e^{j(\omega+\omega_{LO1}-\omega_{LO2})t}]. \quad (7)$$

Note that the frequency components of $\omega-\omega_{LO1}+\omega_{LO2}$ in $s_{IF2,L2/5,I}(t)$ and $s_{IF2,L2/5,Q}(t)$ have opposite polarity. As described later, an appropriate combination of these frequency components and their Hilbert transforms can exhibit different polarities for $\omega > \omega_{LO1}-\omega_{LO2}$ and $\omega < \omega_{LO1}-\omega_{LO2}$. These features are useful for the separation of the L2 and L5 band signals.

To convert the center frequencies of the L1, L2, and L5 band signals to the same IF frequency $f_{IF2}(=\omega_{IF2}/2\pi)$, along the signal path from the first to the second mixers, the LO1 and LO2 frequencies f_{LO1}, f_{LO2} are set as follows:

$$\omega_{LO1} = (\omega_{L1}+\omega_{L2})/2 \quad (8)$$

$$\omega_{LO2} = \omega_{LO1} - (\omega_{L2}+\omega_{L5})/2, \quad (9)$$

where $f_{Li}(=\omega_{Li}/2\pi)$ is the center frequency of the L_i band. In this case, $\omega_{IF2} = (\omega_{L2}-\omega_{L5})/2$. Since $f_{L1} = 1575.42$ MHz, $f_{L2} = 1227.6$ MHz, and $f_{L5} = 1176.45$ MHz, $f_{LO1} = 1401.51$ MHz, $f_{LO2} = 199.485$ MHz, and $f_{IF2} = 25.575$ MHz. In the first down-conversion and the first PPFs, the L1 and L2 band signals are converted to ± 173 MHz images of each other with opposite polarity, as seen in the first and second terms of Eqs. (3) and (4). On the other hand, the L5 band signal is converted to 225.06 MHz during this stage. With regard to the second down-conversion with the following appropriate signal additions, Eq. (5) indicates that $s_{IF2,L1}(t)$ contains the L1 band signal at f_{IF2}. Similarly, Eqs. (6) and (7) reveal that the second terms in $s_{IF2,L2/5,I}(t)$ and $s_{IF2,L2/5,Q}(t)$ contain the L2 and L5 band signals at $\pm f_{IF2}$. These signals are shown graphically in Fig. 3.

To separate each of the L2 and L5 band signals after the second mixing and the following signal additions, the $s_{IF2,L2/5,I}(t)$, $s_{IF2,L2/5,Q}(t)$, and their Hilbert transform generated in the second PPF, which are seen in Fig. 3, are properly manipulated as follows:

$$s_{IF2,L2}(t) = -s_{IF2,L2/5,Q}(t) + H[s_{IF2,L2/5,I}(t)]$$
$$= 2\Im[a(t)e^{j(\omega-\omega_{LO1}+\omega_{LO2})t}]u(\omega_{LO1}-\omega)$$
$$\times u(\omega-\omega_{LO1}+\omega_{LO2})$$
$$- 2\Re[a(t)e^{j(\omega-\omega_{LO1}+\omega_{LO2})t}]u(\omega-\omega_{LO1}) \quad (10)$$

$$s_{IF2,L5}(t) = s_{IF2,L2/5,I}(t) - H[s_{IF2,L2/5,Q}(t)]$$
$$= 2\Re[a(t)e^{j(\omega-\omega_{LO1}+\omega_{LO2})t}]u(\omega_{LO1}-\omega_{LO2}-\omega)$$
$$+ 2\Re[a(t)e^{j(\omega+\omega_{LO1}-\omega_{LO2})t}], \quad (11)$$

where $\omega_{LO1} > \omega_{LO2}$ is utilized to simplify the expressions such that $u(\omega-\omega_{LO1})u(\omega-\omega_{LO1}+\omega_{LO2}) = u(\omega-\omega_{LO1})$. Eqs. (10) and (11) reveal that $s_{IF2,L2}(t)$ and $s_{IF2,L5}(t)$ contain the L2 and L5 band signals at f_{IF2}, respectively, as seen in Fig. 3. The last term in $s_{IF2,L1}(t)$ (Eq. (5)), $s_{IF2,L2}(t)$ (Eq. (10)) and $s_{IF2,L5}(t)$ (Eq. (11)), which corresponds to the higher frequency component, can be filtered out in the following stage (not shown in Fig. 1).

Different from the dual-band reception, the simultaneous triple-band reception requires two frequency conversions. The most important point of the proposed architecture is the use of the same LO1 and LO2 signals for each of triple-band signals to realize the same RF signal delay which is important in some scientific applications (e.g. [2]), as described in Section 1. However, simultaneous generation of the LO1 and LO2 signals using one PLL synthesizer in some literatures [4,5] is impossible. As the simple solution, the LO1 and LO2 signals can be generated using the first PLL with reference frequency f_0 ($=10.23$ MHz) and division ratio 137 and the second PLL with reference $f_0/2$ and division ratio 39, respectively. In addition, the expected sampling frequency in A/D conversion of $s_{IF2,Li}(t)(i=1,2,5)$ is $5f_0$ ($=51.15$ MHz). When the external reference frequency is set to $5f_0$, the LO1, LO2, and the A/D conversion clock signals can be realized using the first and the second PLLs and some frequency dividers. Compared to the literature [8], which uses two PLLs with the same circuit, the proposed architecture requires the first PLL operating at higher frequency and the second PLL operating at lower frequency. The power consumption of the second PLL can be much smaller than that in the first PLL. Thus the first PLL is expected to dominate power consumption for LO generations. To reduce occupation area, the second PLL can use the high-frequency LC VCO with frequency divider instead of low-frequency LC VCO. It means that there is trade-off between occupation area and power consumption in the second PLL, as shown in the literature [16]. By optimizing design of the second PLL, the drawbacks of the proposed architecture in occupation area and power consumption are expected to relax.

3. Circuit design

As mentioned above, the proposed system receives signals on the L1, L2, and L5 triple bands within the frequency range of 1.15–1.6 GHz. This means that the building blocks of the composed system have to be operated during such frequencies. Among these blocks, the LNA is one of the most important blocks. In particular,
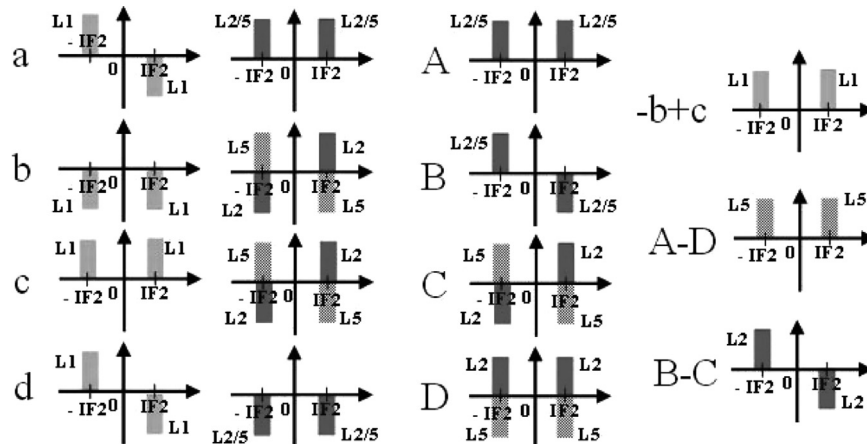

Fig. 3. Conceptual signal spectrum at the locations indicated in Fig. 2.

the LNA that is located at the first stage of the system is applied with a strict frequency characteristic. Usually, the power lever of the GPS signal that enters the antenna is under -90 dBm. Similar to the case with low signal power, the noise characteristic of the system is the most important. In the proposed system, the different band signals are received by using an image-rejection method. Thus, the balance between the signal power and phase is important for canceling unwanted signals.

In this study, a single-ended LNA with an active balun was used to obtain a differential output signal for the first mixer, as shown in Fig. 4 (a). The use of this topology can reduce the phase and amplitude errors of the differential output signals. The LNA is based on a cascode common-source amplifier with inductive source degeneration topology [5]. The use of only a single gain stage reduces the power required and maintains high linearity, and the cascode transistor isolates the input and output ports. The values of the external input inductor L_g and the on-chip inductor L_s are chosen to achieve stable input matching. In contrast to a previous study [5], the quality factor of the load tank circuit is reduced only by using the parasitic resistance of the on-chip inductance L_{Load}. The NF and input reflection coefficient $|S_{11}|$ determine the overall receiver characteristics. The following expressions for NF and $|S_{11}|$ are used:

$$NF \simeq 1 + \frac{\gamma}{\alpha} \cdot \chi(Q_{in}) \cdot \frac{1}{Q_{in}} \cdot \frac{\omega_c}{\omega_T} \tag{12}$$

$$\chi(Q_{in}) = 1 - 2|c|\alpha\sqrt{\frac{\delta}{\kappa\gamma}} + \frac{\delta\alpha^2}{\kappa\gamma}(1 + Q_{in}^2) \tag{13}$$

$$|S_{11}| = \left| \frac{jQ_{in}\left(\frac{\omega}{\omega_c} - \frac{\omega_c}{\omega}\right)}{2 + jQ_{in}\left(\frac{\omega}{\omega_c} - \frac{\omega_c}{\omega}\right)} \right| \tag{14}$$

where R_s is the signal source impedance, $f_c (= \omega_c/2\pi)$ is the center frequency of operating band, $f_T (= \omega_T/2\pi)$ is the unity-current-gain

cutoff frequency of device M_1, Q_{in} is a function of the gate width of M1, which should be chosen to achieve a sufficiently small input reflection [5], α is the ratio of the device transconductance to the zero-bias drain conductance, κ is the Elmore constant, and γ, δ, and c are the drain and induced gate noise current factors and their correlation coefficient, respectively [17,18]. Based on these conditions, Q_{in} can be optimized to achieve a low NF in all three frequency bands for a given current consumption (3 mA in this study).

Fig. 4(b) and (c) shows circuit schematics for the first and second mixers. To improve the linearity in a wide-band GPS system, the transconductance stage in the first mixer includes source degeneration. In contrast to our previous work [12,13], a shared transconductor is not used in the first mixer because the IMRR can also be improved in the IF analog circuit blocks [19] or when applying the digital compensation technique described in Section 5. The quadrature LO generator shown in Fig. 4(d) is used for the first and second mixing processes. Two-stage PPF is useful to enhance the robustness of the process variations in passive elements [20].

4. Experimental results

The proposed system was verified by using a 130 nm eight-metal RF CMOS process. A photograph of the fabricated chip is shown in Fig. 5. The area of the chip, including the input and output pads, is about 2.4 mm². The power consumption of the system is approximately 7.2 mW with a 1.2 V supply voltage, which is mainly supplied to the LNA and mixers. The designed chip has no external inductor (L_g in Fig. 4(a)) to dominate the input matching. The inductance of L_g is too large (8.2 nH) to be integrated into the chip. For good input matching in the packaged chip, an external inductor that utilizes bonding wire is used for L_g.

The chip-level measurement was firstly carried out using a wafer probe station. Rather than an external inductor, a manual tuner was used to measure the input matching at each narrow band. To obtain
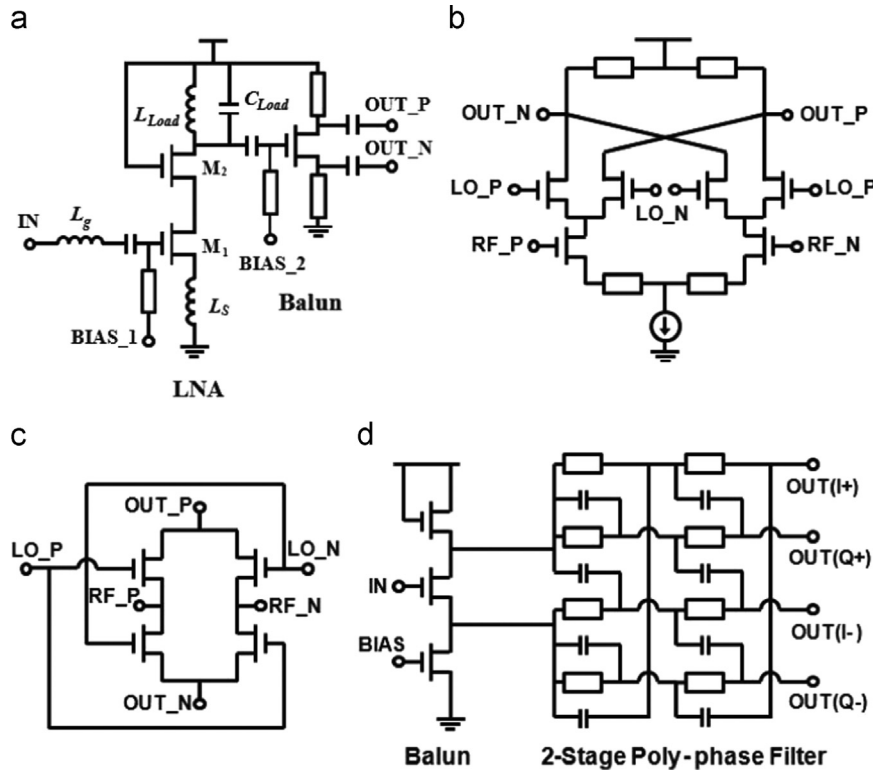

Fig. 4. Schematic diagram of the (a) LNA, (b) first mixer, (c) second mixer, and (d) the quadrature LO generator that were designed in this study.
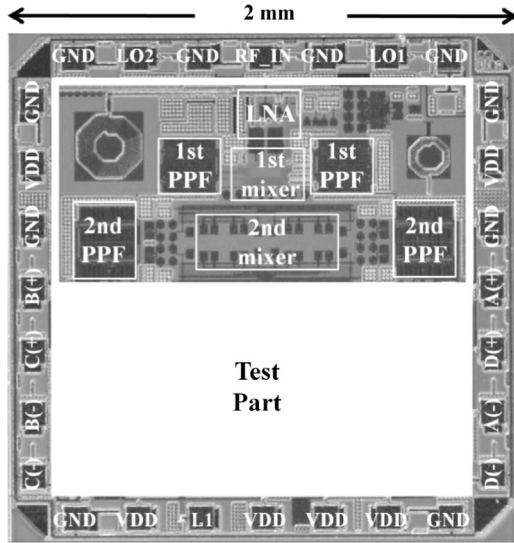
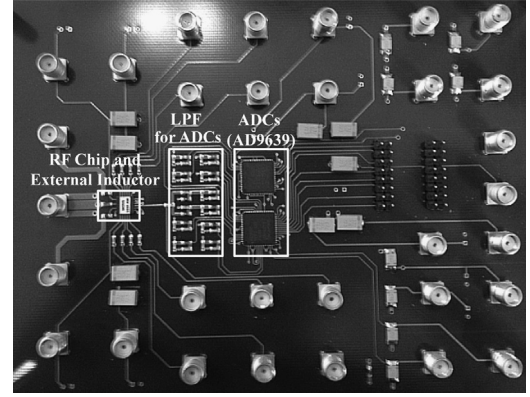Fig. 5. Optical micrograph of the fabricated chip.
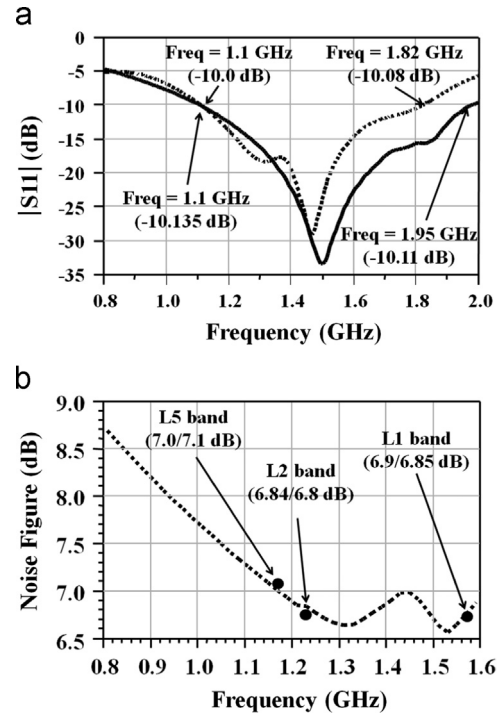

Fig. 6. A photo of the fabricated module.

Fig. 7. (a) $|S_{11}|$ of the chip (solid line) and module (dotted line). (b) NF of the chip (closed mark) and module (dotted line).

the expected characteristics from the chip-level measurement data, the insertion loss of the tuner, cables, and probe needle are compensated from the data [21], and the small-signal and noise characteristics of the receiver chip with an ideal inductor L_g in series with the gate of M1 can thus be estimated [22]. This evaluation process avoids instrumental errors originating from the bonding wires in the packaged chip. The NF and S11 of the system were measured with these compensated conditions. A more detailed description of this compensated method is described in Appendices A and B.

Based on the chip-level measured data, a promising value of the external inductor can be precisely obtained. Although the simultaneous triple-band reception was not demonstrated due to the narrow-band input matching described in the previous study [11], the use of an external inductor with bonding wire for L_g on the test module enables such reception due to the wide-band input matching. A module that demonstrates triple-band GPS reception was designed and fabricated as shown in Fig. 6. In addition to the chip packaged in a 24-pin QFN package and the external inductor for input matching, the module has A/D converters (ADCs) for observing the received data on a specific time domain and anti-alias IF passive low-pass filters (passband loss: $\sim$1 dB; 3 dB-bandwidth: 25 MHz). In this study, commercial ADCs (AD9639) are used. The subtractors of the signals at A and D and those at B and C in Fig. 2 were implemented by using a precise power splitter (Agilent 11667B, 50 $\pm$ 2 Ω) in the previous study [11]. In this study, the same functions for the ADC input signals are implemented by using precise external resistances ($\sim$1 kΩ) on the module, which provide much higher load resistances of the second PPFs ($\sim$200 Ω resistances are used) in addition to the ADC input resistances (4.3 kΩ) and have little influence on the IMRR in this design, as described in Appendix C. The L1 port at the lower part of Fig. 5 outputs sigle-end L1 band signal, which is one of differential L1 band signal. This results in the same gain for the L1, L2, and L5 band signals, as seen in Fig. 8 later. An off-chip balun is used to restore the differential L1 band signal as one of ADC input.

Fig. 7 shows the measurement results for S_{11} and the NF of the chip and module. The input matching of the module is slightly narrower than that of the chip, which originates from the parasitic elements of the external inductor that was used in the module for input matching. Fortunately, it does not matter because an input reflection under -10 dB is guaranteed for the desired L1, L2, and L5 frequency bands. In addition, the NF data of the module show good agreement with those of the chip at the L1, L2, and L5 bands. The measured NF is less than 7.0 dB for the desired frequency range covering the L1, L2, and L5 bands.

In the previous work [11], only each of unmodulated signals was used to show the capability of the triple-band reception due to narrow-band input matching in the manual tuner. The module fabricated in this study can demonstrate simultaneous triple-band reception thanks to the good wide-band input matching. Fig. 8 shows the measurement results of the received IF signals of the fabricated module. To investigate the capability of the chip for triple-band reception, the input signals have the triple-band signals shown in Fig. 8(a). To distinguish each of the received signals, the modulated frequency is set differently for each band. The L1 band signal is CW, and the BPSK modulation frequencies of the L2 and L5 band signals are 5 MHz and 2.5 MHz, respectively. The level of the input signals is around -75 dBm, which corresponds to the typical GPS signal level in the active antenna output. The power of the LO1 and LO2 signals is 5 dBm. The output signal power level is found to be about -50 dBm. As seen in Fig. 8 (b), each band signal can be separated from the other signals and received on the desired port. Without any compensation at the IF port, the IMRR for the L1 and other signals (L2 and L5) is 40 dB and that for L2 and L5 is 37–38 dB.

Fig. 9 shows the digital output signals of the ADC in the module. The data rates of the modulated signals are different to verify the received data at each port. The L1, L2, and L5 band signals are modulated with BPSK at 10 MHz, 5 MHz, and 2.5 MHz, respectively. The left side of Fig. 9 shows the input signals that were measured directly on the signal generator, and the right side shows the measured output signals of the ADCs. The ADC sampling period is 5 ns to capture the waveforms although the expected A/D conversion rate is 51.15 MS/s in the real applications as described in Section 2. This figure implies that the data rates of the measured signals at the L1, L2, and L5 ports are 10 MHz, 5 MHz, and 2.5 MHz, respectively.

5. Discussion on the IMRR improvement technique

As seen in Fig. 1, the L1 band signal is received through the first PPF, while the L2 and L5 band signals are received through the first and second PPFs. The mismatch in the second PPF degrades the
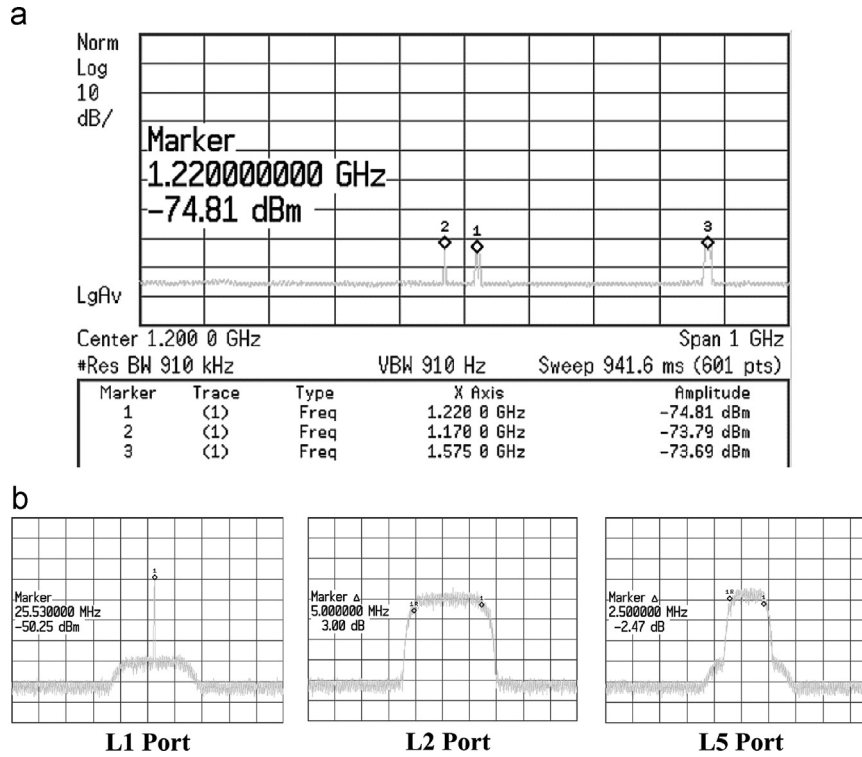

Fig. 8. (a) Triple-band RF signals (L1: CW, L2: 5 MHz BPSK modulation, L5: 2.5 MHz BPSK modulation) and (b) the received IF signals at each port.
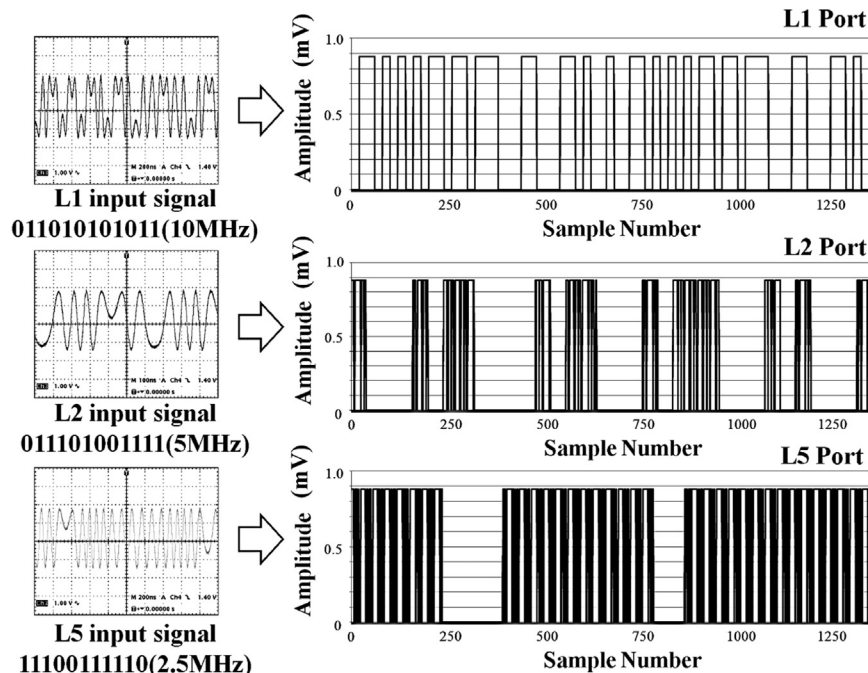

Fig. 9. Modulated RF input signals and ADC 2-b binary output signals (LSB: ∼439 μV) in the fabricated module.

IMRR for the L2 and L5 band signals. From the measurement results, the IMRR between the L1 and other band signals is 40 dB, while that of between the L2 and L5 band signals is 37–38 dB.

The degraded IMRR between the L2 and L5 bands can be compensated by using an analog or digital technique [19,23]. To avoid large area occupation and high power consumption, the digital compensation of the IMRR for the ADC outputs is investigated. In this technique, the relation of the signals at A and D and those at B and C in Fig. 2 is implemented digitally by using four ADCs, which is two more than those used for the evaluation module described in the previous section. As the AD9639 used in this work has four ADCs inside, the two ADC components embedded on the module (total eight ADCs) can afford for evaluation of this digital compensation. As described later, the required bit number of the ADC is four. To provide signal with adequate level to each of the ADC inputs, the differential probes (Tektronix P6247, attenuation 10:1) were used as IF amplifiers in this work.

The block diagram of the digital compensation is conceptually shown in Fig. 10. For digital compensation technique, it is important to detect any amplitude and phase errors. Phase errors are more significant than amplitude errors since GPS receivers usually use low-resolution ADCs. This suggests that the amplitude errors of the L2 and L5 band signals in the second PPF can experience quantization errors from the ADC. From the circuit simulation results, the phase error of the L2 and L5 band signals is around $5°$. The target of the following detectable phase error is set to a few degrees:

$$\text{Detectable Phase Error} \approx \frac{2\pi/M}{2^n} \tag{15}$$

Here M is the ratio of the ADC sampling rate to the target frequency, and n is the effective number of bits of the ADC for the input level. For a 4-bit ADC with 200 MS/s sampling rate, a phase error under $5°$ can be detected for a 25 MHz IF signal with a resolution of a few degrees.

The $I(t)$ and $Q(t)$ signals in Fig. 10 are as follows:

$$I(t) = m(t)\ \cos(\omega_{IF2}\ t) \tag{16}$$

$$Q(t) = a_e m(t)\ \sin(\omega_{IF2}\ t + \theta_e), \tag{17}$$

where a_e is the amplitude error, θ_e is the phase error between the $I(t)$ and $Q(t)$ signals. When $a_e = 1$ and $\theta_e = 0$, $Q(t) = H[I(t)]$. For compensation in $s_{IF2,L5}(t)$ in Fig. 2, $I(t)$ and $Q(t)$ correspond to the second terms in Eqs. (6) and (7), respectively. Similarly, to compensate for $s_{IF2,L2}(t)$ in Fig. 2, $I(t)$ and $Q(t)$ correspond to the second terms in Eqs. (6) and (7) with phases advanced by $\pi/2$, respectively. To obtain the phase error between the $I(t)$ and $Q(t)$ signals, a multiplier with a gain of 2 (6 dB) is used for the initial condition of $a_e = 1$, and its output is integrated in a single period to pass a low-frequency error component related to the compensation factors ($\sin\theta_e$, $\cos\theta_e$, and a_e in Eq. (18)). From the calculation using the feed-back loop in Fig. 10, a compensated signal can be obtained as follows:

$$Q_{comp}(t) = \frac{Q(t)}{a_e\cos\theta_e} - I(t)\tan\theta_e = m(t)\ \sin(\omega_{IF2}\ t) \tag{18}$$
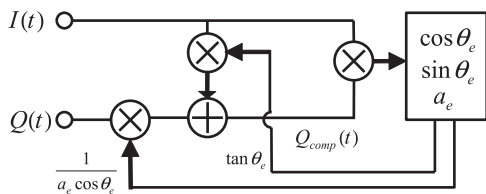

Fig. 10. Block diagram of the phase and amplitude compensation.

Utilizing $I(t) - H[Q_{comp}(t)]$ instead of $I(t) - H[Q(t)]$ can improve the IMRR. To improve the IMRR at the L5 port, $I(t)$ and $Q(t)$ are assigned to the signals at A and C in Fig. 2, and $H[Q_{comp}(t)]$ can be obtained in the following digital signal precessing:

$$H[Q_{comp}(t)] = \frac{H[Q(t)]}{a_e\cos\theta_e} - \tan\theta_e\ H[I(t)] \approx \frac{H[Q(t)]}{a_e\cos\theta_e} + \tan\theta_e\ H[H[Q(t)]] \tag{19}$$

The Hilbert transform can be calculated simply with the delay by a quarter of signal period in over-sampled digital signal data. Based on the above approximated formula, the approximated signal of $H[Q_{comp}(t)]$ can be calculated from only $H[Q(t)]$ (the signal at D in Fig. 2) after obtaining a_e and θ_e. L2 band signal also can be improved in the same way.

To verify the digital compensation technique for the L5 port, the ADC outputs at A and D in Fig. 2 were measured. The phase error, θ_e, can be obtained from the ADC outputs at A and D in Fig. 2 in the following. $I(t)$ in Fig. 10 corresponds to the signal at A. Considering interconnection modifications on the board, the inverse Hilbert transform ($H^{-1}[\cdot] = -H[\cdot]$) of the signal at D was used as $Q(t)$ instead of that at C. As a result, the $Q_{comp}(t)$ and $H[Q_{comp}(t)]$ signals are approximately calculated only from the ADC output at D using Eq. (19).

The amplitude error can be compensated for after this phase error compensation. By considering amplitude errors on Eqs. (6) and (7), the signals at A and D ($s_A(t)$ and $s_D(t)$) are expressed as

$$s_A(t) = m_{L2}(t)\cos(\omega_{IF2}t + \theta) + m_{L5}(t)\cos(\omega_{IF2}t), \tag{20}$$

$$s_D(t) = (1 + \varepsilon_1)\ m_{L2}(t)\cos(\omega_{IF2}t + \theta) - (1 + \varepsilon_2)\ m_{L5}(t)\cos(\omega_{IF2}t), \tag{21}$$

where θ means phase difference between the L2 and L5 band signals, and $|\varepsilon_1|, |\varepsilon_2| \ll 1$. Considering $s_A(t) - s_D(t)$ based on the above expressions, the IMRR for L5 port without the digital amplitude error compensation is given by $|(2 + \varepsilon_2)/\varepsilon_1|^2 \approx 4/\varepsilon_1^2$. To compensate the amplitude error, the following calculation with small compensation parameter ε_1' is used:

$$\begin{aligned} s_A(t) &- (1 - \varepsilon_1')s_D(t) \\ &\approx (\varepsilon_1' - \varepsilon_1)\ m_{L2}(t)\cos(\omega_{IF2}t + \theta) \\ &+ (2 + \varepsilon_2 - \varepsilon_1')\ m_{L5}(t)\cos(\omega_{IF2}t) \end{aligned} \tag{22}$$

In this case, the IMRR for L5 port is given by $|(2 + \varepsilon_2 - \varepsilon_1')/(\varepsilon_1' - \varepsilon_1)|^2 \approx 4/|\varepsilon_1' - \varepsilon_1|^2$. By setting $\varepsilon_1' = \varepsilon_1$, the IMRR can be improved well. The IMRR for the L2 port can be improved in the same way using the signals at B and C in Fig. 2.

From the measurement results, we obtain ε_1 and ε_2 as 0.0252 (-31.9 dB) and 0.0266 (-31.5 dB). By setting $\varepsilon_1' = \varepsilon_1$ with these conditions, the IMRR between the L2 and L5 band signals becomes approximately 49 dB. Fig. 11 shows measured result where the
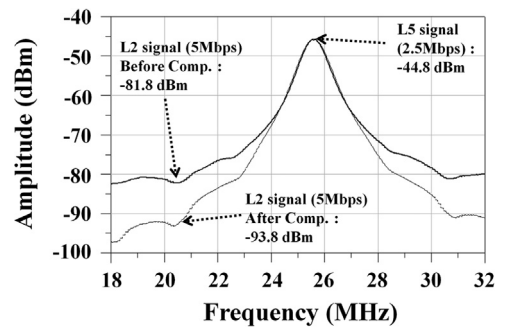

Fig. 11. Signal spectrum at the L5 port with IMRR correction (dotted line) and without IMRR correction (solid line). The obtained FFT data are processed through band-pass filtering (center frequency: 25.595 MHz, pass-band width: 10 MHz, pass-band ripple: 0.01 dB) and 61-point moving averaging.

BPSK modulation signals of 5 MHz and 2.5 MHz modulation frequency are used for L2 and L5 band signals, respectively. To ensure the IMRR improvement, the obtained FFT data are processed through band-pass filtering and moving averaging. As a result, an improvement of around 12 dB of IMRR between the L2 and L5 band signals is observed by using the digital compensation technique described above. In this experiment, at least a 4-bit ADC was required to detect a phase error of under 3° at the second PPF outputs. Although a 4-bit ADC may be a little heavy for GPS applications, the allowable mismatches in the PPFs can be relaxed.

6. Conclusion

In this paper, a receiver that uses two local oscillators was proposed for the simultaneous triple-band reception of the L1, L2, and L5 GPS signals. The proposed receiver was designed in a 130 nm CMOS process to demonstrate the possibility of concurrent triple-band reception with a modified Weaver image-rejection technique. For each of the output ports, the IMRR was estimated to be 37–40 dB. By using the proposed digital compensation process, an estimated IMRR of 49 dB can be obtained.

Although the present research is a preliminary study and further work is required before our device can be used in practical applications, the feasibility of simultaneous GPS triple-band reception with a single RF path has been demonstrated.

Acknowledgments

Appendix A. Excess noise ratio with compensation of signal loss

Fig. A1 shows a block diagram of the chip-level NF measurements with a wafer probe station, which has a probe needle, cable, and a manual tuner for input matching. To evaluate the performance of the chip, while including the loss of the pad, the loss from the signal source to the surface of the chip's pad must be compensated. When measuring the NF, a reference point of the controllable noise source with a known excess noise ratio (ENR) (port $1-1'$ in Fig. A1) must be changed to the surface of the chip's pad (port $2-2'$ in Fig. A1). This effectively changes the ENR used in the NF measurement.
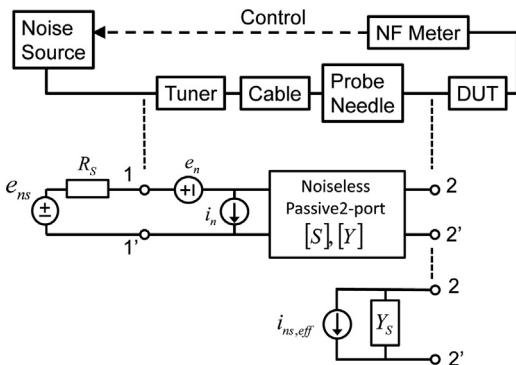

Fig. A1. Chip-level NF measurement block diagram with the equivalent passive blocks.

The available noise power of the controllable noise source during the off-state and on-state is expressed as $k_B T_{off} \Delta f$ and $k_B T_{on} \Delta f$, respectively. Here, k_B is the Boltzmann constant, Δf is the bandwidth, and T_{off} and T_{on} are the equivalent absolute temperatures used to express the off-state and on-state noises, respectively. Using the noise source resistance R_S, the corresponding noise voltages $e_{ns,off}$ and $e_{ns,on}$ are given by

$$\overline{|e_{ns,off}|^2} = 4k_B T_{off} R_S \Delta f \tag{A.1}$$

$$\overline{|e_{ns,on}|^2} = 4k_B T_{on} R_S \Delta f \tag{A.2}$$

The ENR value is defined as follows:

$$ENR = \frac{\overline{|e_{ns,on}|^2} - \overline{|e_{ns,off}|^2}}{\overline{|e_{ns,off}|^2}} = \frac{T_{on} - T_{off}}{T_{off}} \tag{A.3}$$

Noise figure NF can be obtained by using the ENR as follows:

$$NF = \frac{ENR}{Y - 1}, \tag{A.4}$$

where the Y factor is defined as the ratio of the noise power measured at the output for the on-state and off-state noise sources.

To calculate the effective value of the ENR with reference port $2-2'$ in Fig. A1 (ENR_{eff}), the passive 2-port block from the signal source to the surface of the chip's pad is focused. The correlation matrix of the noise waves at both ports in the passive 2-port block at absolute temperature T is expressed as

$$[C_S] = k_B T([E] - [S][S^\dagger]), \tag{A.5}$$

where $[E]$ is the unit matrix and $[S]$ is the scattering matrix of this block [24,25]. Using this equation, the correlation matrix of the input-referred noise voltage e_n and current i_n can be obtained from $[C_S]$ as follows:

$$[C_A] = \frac{1}{\Delta f} \begin{bmatrix} \overline{|e_n|^2} & \overline{e_n i_n^*} \\ \overline{e_n^* i_n} & \overline{|i_n|^2} \end{bmatrix} = [T][C_Y][T^\dagger], \tag{A.6}$$

$$[C_Y] = ([E] + Z_0[Y])[C_S]([E] + Z_0[Y^\dagger]), \tag{A.7}$$

where $[Y]$ is the admittance matrix of this block, Z_0 is the characteristic impedance, and $[T]$ is the transformation matrix from the admittance representation $[C_Y]$ to the chain representation $[C_A]$ [26]. By using elements of $[C_A]$ calculated by the above equations, ENR_{eff} can be expressed as follows:

$$\begin{aligned} ENR_{eff} &= \frac{\overline{|e_{ns,on} + e_n + i_n R_S|^2} - \overline{|e_{ns,off} + e_n + i_n R_S|^2}}{\overline{|e_{ns,off} + e_n + i_n R_S|^2}} \\ &= \frac{ENR}{1 + \overline{|e_n + i_n R_S|^2}/4R_S k_B T_{off} \Delta f} \end{aligned} \tag{A.8}$$

The value of ENR_{eff} can be calculated by using the ENR, R_S, and the elements of $[C_A]$. By using ENR_{eff} instead of ENR in Eq. (A.4), the NF with loss compensated from the signal source to the surface of the chip's pad can be obtained.

Appendix B. NF re-calculation with the external inductor

To estimate the NF value with the external inductor, the noise parameters are required. The NF for source admittance Y_S seen from the surface of the chip pad is given by

$$NF = NF_{min} + \frac{R_n}{\text{Re}[Y_S]} |Y_S - Y_{opt}|^2, \tag{B.1}$$

where the noise parameters NF_{min}, R_n, and Y_{opt} are the minimum NF, noise resistance, and optimum source admittance, respectively. These noise parameters can be obtained from the NF values
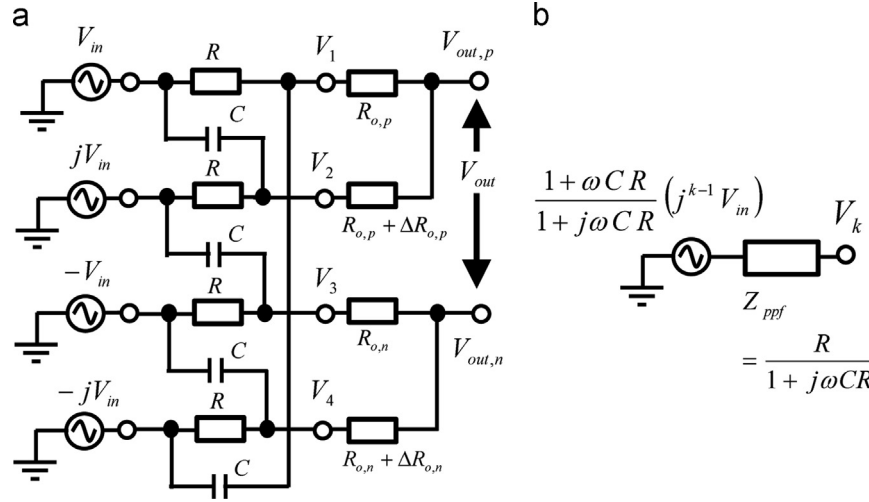
Fig. C1. (a) Simple PPF with resistive adder and (b) equivalent circuit to calculate $V_k(k=1,2,3,4)$.

obtained for various Y_S values by using the manual tuner. The source admittance Y_S seen from the surface of the chip pad can be obtained by using scattering parameters [S] of the passive 2-port block from the signal source described in Appendix A. When the impedance of the signal generator is approximated to Z_0, $Y_S \approx (1/Z_0)(1-S_{22})/(1+S_{22})$.

To re-calculate the NF value with the external input inductor $L_{g,ext}$ based on the noise parameters, the following equation for Y_S is used:

$$Y_{S\ \text{withext.ind.}} = (Z_0 + j\omega L_{g,ext})^{-1}, \tag{B.2}$$

where the impedance of the signal source is set to the characteristic impedance Z_0.

Appendix C. Influence of PPF's load on IMRR

For simplification, the one-stage PPF shown in Fig. C1(a) is considered with mismatch in resistive adders ($\Delta R_{o,p}, \Delta R_{o,n}$). By using the equivalent circuit in Fig. C1(b) to obtain V_k ($k=1,2,3,4$), $V_{out,p}/V_{in}$ is given by

$$\frac{V_{out,p}}{V_{in}} = \frac{1+\omega CR}{1+j\omega CR}\frac{(1+j)(Z_{ppf}+R_{o,p})+\Delta R_{o,p}}{2(Z_{ppf}+R_{o,p})+\Delta R_{o,p}}$$
$$\approx \frac{1+j}{2}\frac{1+\omega CR}{1+j\omega CR}\left(1-\frac{j}{2}\frac{\Delta R_{o,p}}{Z_{ppf}+R_{o,p}}\right). \tag{C.1}$$

As $V_{out,n}$ can be obtained similarly, V_{out}/V_{in} is expressed as follows:

$$\frac{V_{out}}{V_{in}} \approx \frac{1+j}{2}\frac{1+\omega CR}{1+j\omega CR}\left[1-\frac{j}{2}\left(\frac{\Delta R_{o,p}}{Z_{ppf}+R_{o,p}}+\frac{\Delta R_{o,n}}{Z_{ppf}+R_{o,n}}\right)\right] \tag{C.2}$$

The factor $1+\omega CR$ means image-rejection and it is not influenced by mismatch in resistive adders.

References

[1] T. Kadoyama, N. Suzuki, N. Sasho, H. Iizuka, I. Nagase, H. Usukubo, M. Katakura, A complete single-chip GPS receiver with 1.6-V 24-mW radio in 0.18-μm CMOS, IEEE J. Solid-State Circuits 39 (April (4)) (2004) 562–568.
[2] T. Ebinuma, A. Yasuda, Airborne GPS reflectometry from low altitude aircraft, SICE J. Control, Meas., Syst. Integr. 3 (November (6)) (2010) 429–434.
[3] S. Gunawardena, Z. Zhu, M. Braasch, Observing the GPS L5 Test Transmission from SVN49 Using Software Radio Processing, Inside GNSS 4 (May/June (3)) (2009) 22–29.
[4] J. Ko, J. Kim, S. Cho, K. Lee, A 19 mW 2.6 mm² L1/L2 dual band CMOS GPS receiver, IEEE J. Solid-State Circuits 40 (July (7)) (2005) 1414–1424.
[5] Y. Utsurogi, M. Haruoka, T. Matsuoka, K. Taniguchi, CMOS front-end circuits of dual-band GPS receiver, IEICE Trans. Electron. E88-C (June (6)) (2005) 1275–1279.
[6] M. Detratti, E. López, E. Pérez, R. Palacio, Dual-band RF front-end solution for hybrid Galileo/GPS mass market receivers, in: 5th IEEE Consumer Communications and Networking Conference (CCNC 2008), January 2008, pp. 603–607.
[7] J. Wu, P. Jiang, D. Chen, J. Zhou, A dual-band GNSS RF front end with a pseudo-differential LNA, IEEE Trans. Circuits Syst. 58 (March (3)) (2011) 134–138.
[8] D. Chen, W. Pan, P. Jiang, J. Jin, T. Mo, J. Zhou, Reconfigurable dual-channel multiband RF receiver for GPS/Galileo/BD-2 systems, IEEE Trans. Microw. Theory Techn. 60 (November (11)) (2012) 3491–3501.
[9] T. Elesseily, T. Ali, K. Sharaf, A crystal-tolerant fully integrated CMOS low-IF dual-band GPS receiver, Analog Integr. Circuits Signal Process. 63 (May (2)) (2010) 143–159.
[10] J. Li, D. Chen, R. Guan, P. Qin, Z. Lu, J. Zhou, Low-power high-linearity area-efficient multi-mode GNSS RF receiver in 40 nm CMOS, in: IEEE International Symposium on Circuits and Systems(ISCAS), May 2012, pp. 1291–1294.
[11] I. Jo, J. Bae, T. Matsuoka, T. Ebinuma, Design of triple-band CMOS GPS receiver RF front-end, IEICE Electron. Express 10 (April (7)) (2013) 20130126.
[12] M. Haruoka, Y. Utsurogi, T. Matsuoka, K. Taniguchi, A study on the LO phase error compensation of GPS dual-band image-reject mixer, IEICE Trans. Electron. J86-C (November (11)) (2003) 1177–1183.
[13] M. Haruoka, Y. Utsurogi, T. Matsuoka, K. Taniguchi, A study on the LO phase error compensation of GPS dual-band image-reject mixer, Electron. Commun. Jpn., Part 2 88 (December (12)) (2005) 26–33.
[14] K.W. Martin, Complex Signal Processing is Not Complex, IEEE Trans. Circuits and Systems—I 51 (September (9)) (2004) 1823–1836.
[15] B. Boashash, Estimating and interpreting the instantaneous frequency of a signal. Part I. Fundamentals, Proc. IEEE 80 (April (4)) (1992) 520–538.
[16] S. Hara, R. Murakami, K. Okada, A. Matsuzawa, The optimum design methodology of low-phase-noise LC-VCO using multiple-divide technique, IEICE Trans. Fundam. E93-A (February (2)) (2010) 424–430.
[17] D.K. Shaeffer, T.H. Lee, A 1.5-V, 1.5-GHz CMOS low noise amplifier, IEEE J. Solid-State Circuits 32 (May (5)) (1997) 745–759.
[18] D.K. Shaeffer, T.H. Lee, Corrections to A 1.5-V, 1.5-GHz CMOS low noise amplifier, IEEE J. Solid-State Circuits 40 (May (6)) (2005) 1397–1398.
[19] T. Kamata, K. Okui, M. Fukasawa, T. Matsuoka, K. Taniguchi, Low-power zero-IF full-segment ISDB-T CMOS tuner with tenth-order baseband filters, IEEE Trans. Consum. Electron. 57 (May (2)) (2011) 403–410.
[20] F. Behbahani, Y. Kishigami, J. Leete, A.A. Abidi, CMOS mixers and polyphase filters for large image rejection, IEEE J. Solid-State Circuits 36 (June (6)) (2001) 873–887.
[21] B. Wei, Y. Dai, J. Wang, T. Matsuoka, K. Taniguchi, Design of a low-voltage CMOS mixer based on variable load technique, IEICE Electron. Express 7 (April (7)) (2010) 473–479.
[22] G. Kim, B. Murakami, M. Goto, T. Kihara, K. Nakamura, Y. Shimizu, T. Matsuoka, K. Taniguchi, Small-signal and noise model of FD-SOI MOS devices for low noise amplifier, Jpn. J. Appl. Phys. 45 (September (9A)) (2006) 6872–6877.
[23] T. Nicolay, M. Buchholz, M. Gross, Baseband signal processing of digital video broadcasting direct-conversion zero-IF tuners, IEEE Trans. Consum. Electron. 51 (February (1)) (2005) 48–53.
[24] S. Wdege, D. Rutledge, Noise waves and passive linear multiports, IEEE Microw. Guided Wave Lett. 1 (May (5)) (1991) 117–119.
[25] S. Wdege, D. Rutledge, Wave techniques for noise modeling and measurement, IEEE Trans. Microwave Theory Tech. 40 (November (11)) (1992) 2004–2012.
[26] H. Hillbrand, P. Russer, An efficient method for computer aided noise analysis of linear amplifier networks, IEEE Trans. Circuits Syst. 23 (April (4)) (1976) 235–238.